CHEMISTRY OF MATERIALS

ARTICLE

pubs.acs.org/cm

Polyimide Aerogels by Ring-Opening Metathesis Polymerization (ROMP)

Nicholas Leventis,*[,†] Chariklia Sotiriou-Leventis,*[,†] Dhairyashil P. Mohite,[†] Zachary J. Larimore,[‡] Joseph T. Mang,*[,§] Gitogo Churu,[⊥] and Hongbing Lu*[,⊥]

[†]Department of Chemistry, Missouri University of Science and Technology, Rolla, Missouri 65409, United States

[‡]Department of Mechanical Engineering, Missouri University of Science and Technology, Rolla, Missouri 65409, United States

[§]Los Alamos National Laboratory, Los Alamos, New Mexico 87545, United States

[⊥]Department of Mechanical Engineering, The University of Texas at Dallas, Richardson, Texas 75080, United States

ABSTRACT: Polyimide aerogel monoliths are prepared by ring-opening metathesis polymerization (ROMP) of a norbornene end-capped diimide, **bis-NAD**, obtained as the condensation product of nadic anhydride with 4,4′-methylenedianiline. The density of the material was varied in the range of 0.13−0.66 g cm^{-3} by varying the concentration of **bis-NAD** in the sol. Wet gels experience significant shrinkage, relative to their molds (28%−39% in linear dimensions), but the final aerogels retain high porosities (50%−90% v/v), high surface areas (210−632 m^2 g^{-1}, of which up to 25% is traced to micropores), and pore size distributions in the mesoporous range (20−33 nm). The skeletal framework consists of primary particles 16−17 nm in diameter, assembling to form secondary aggregates (by SANS and SEM) 60−85 nm in diameter. At lower densities (e.g., 0.26 g cm^{-3}), secondary particles are mass fractals (D_m = 2.34 ± 0.03) turning to closed-packed surface fractal objects (D_S = 3.0) as the bulk density increases (≥0.34 g cm^{-3}), suggesting a change in the network-forming mechanism from diffusion-limited aggregation of primary particles to a space-filling bond percolation model. The new materials combine facile one-step synthesis with heat resistance up to 200 °C, high mechanical compressive strength and specific energy absorption (168 MPa and 50 J g^{-1}, respectively, at 0.39 g cm^{-3} and 88% ultimate strain), low speed of sound (351 m s^{-1} at 0.39 g cm^{-3}) and styrofoam-like thermal conductivity (0.031 W m^{-1} K^{-1} at 0.34 g cm^{-3} and 25 °C); hence, they are reasonable multifunctional candidate materials for further exploration as thermal/acoustic insulation at elevated temperatures.

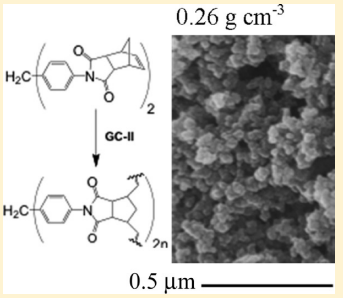

KEYWORDS: ROMP, norbornene, end-capped, polyimides, aerogels

1. INTRODUCTION

Aerogels are low-density nanoporous solids with high surface area, low thermal conductivity, and high acoustic attenuation.[1,2] They are prepared by converting and removing the pore-filling solvents of suitable wet gels as supercritical fluids (SCFs).[3,4] Inorganic aerogels are mostly based on silica and have been studied more extensively. They are fragile materials, and confirmed applications have been only in specialized environments (for example, as thermal insulators aboard planetary vehicles and as Cherenkov radiation detectors in certain nuclear reactors). Other oxide aerogels are evaluated as energetic materials, or starting materials for porous metals and ceramics.[5−7]

On the other hand, organic aerogels were first reported together with the inorganic counterparts;[3,4] however, early emphasis on the latter delayed their systematic investigation for almost 60 years, until Pekala reported the bottom-up synthesis of phenolic resin-type aerogels via condensation of resorcinol with formaldehyde (RF).[8] Subsequently, several other types of bottom-up polymer aerogels were reported, first by variation of the phenolic resin chemistry (phenol−furfural,[9] cresol−formaldehyde,[10] melamine−formaldehyde[11]), and then based on polyurethane,[12] polyurea,[13] and, more recently, polybenzoxazine,[14] poly(bicyclopentadiene) synthesized via ring-opening metathesis polymerization (ROMP) of the monomer,[15] and polyimides.[16,17] Several other types of aerogels based on soluble polymers such as polystyrene,[18] polyacrylonitrile,[19] and cellulose[20] are prepared by inducing phase separation of preformed polymers. The accelerated interest in organic aerogels is driven by the facile tailoring of their properties by choosing the polymer, the straightforwardness of the polymerization process that facilitates synthesis, and the fact that inorganic aerogels, whose skeletal framework has been cross-linked covalently by a conformal polymer coating, demonstrate dramatically increased mechanical strength, rendering this class of materials suitable for applications previously inconceivable for aerogels for example, in ballistic protection (armor).[21] Since the mechanical properties of the latter materials are dominated by the polymer, purely polymeric aerogels with the structure and interparticle connectivity of polymer-cross-linked aerogels should have similar mechanical properties.

In that context, interest in polyimide aerogels stems from the high mechanical strength and high thermal stability of the polymer,[22] which would render this class of aerogels suitable for high-temperature thermal and acoustic insulation. In general,

Received: February 1, 2011
Revised: March 12, 2011
Published: March 30, 2011

Table 1. Formulations of bis-NAD-xx Aerogels

sample	**bis-NAD** (% w/w versus NMP)	**GC-II** (% w/w versus **bis-NAD**)	**GC-II** (% mol versus **bis-NAD**)	**bis-NAD**: **GC-II** (mol:mol)
bis-NAD-2.5	2.5	4.0	2.30	43.3
bis-NAD-5	5.0	2.0	1.15	86.6
bis-NAD-10	10.0	1.0	0.58	173.2
bis-NAD-15	15.0	0.75	0.43	231.0
bis-NAD-20	20.0	0.50	0.29	346.4

there are two classic routes to consider for polyimide aerogel synthesis: the first (DuPont process) yields linear polyimides and involves reaction of dianhydrides with diamines,[23] whereas the second one, which is referenced as the polymerization of monomeric reactants (PMR) route yields thermoset resins and involves the synthesis and polymerization of norbornene-capped imide oligomers.[24] The DuPont route proceeds through a linear polyamic acid that is dehydrated to the imide either chemically (e.g., with sacrificial reagents such as acetic anhydride/pyridine), or thermally at high temperatures. The PMR route has been strictly a high-temperature process involving cross-linking of the norbornene end-caps.

The first polyimide aerogels were prepared via the DuPont process, using both chemical dehydration and high-temperature treatment to complete imidization.[16,17,25] Those conditions compound the inherent economic disadvantage of supercritical fluids in the aerogel synthesis. In that regard, recently, we introduced an alternative route whereas polyimide aerogels can be obtained at room temperature via reaction of dianhydrides with diisocyanates; thus, aerogels prepared from pyromellitic dianhydride and 4,4′-methylenedianiline are chemically identical to those prepared from the same anhydride and methylene diphenyl-*p*-diisocyanate.[26] Here, we introduce a second low-temperature process to polyimide aerogels via the PMR route, whereas the norbornene end-caps of a suitable bisnadimide, **bis-NAD**, are polymerized via ROMP using the second-generation Grubbs' catalysts **GC-II**.[27] Evidently, **bis-NAD**-derived polyimide aerogels are extremely robust multifunctional materials, combining styrofoam-like thermal conductivity and mechanical properties comparable to those of polymer-cross-linked silica aerogels.[21]

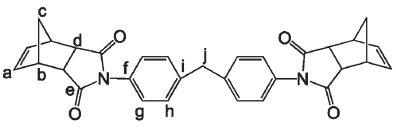

bis-NAD

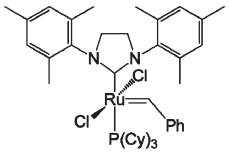

GC-II

2. EXPERIMENTAL SECTION

2.1. Materials. All reagents and solvents were used as received, unless noted otherwise. Dicyclopentadiene (DCPD), a second-generation Grubbs' catalyst, **GC-II**, and anhydrous *N*-methyl-2-pyrrolidone (NMP) were purchased from Aldrich Chemical Co. Maleic anhydride, 4,4′-methylenedianiline (MDA), and 1,4-dioxane were purchased from Acros Organics. Methanol and laboratory-grade NMP were purchased from Fisher.

2.2. Synthesis of bis-NAD. Bis-NAD [IUPAC name: 2,2′-(methylenebis(4,1-phenylene))bis(3a,4,7,7a-tetrahydro-1*H*-4,7-methanoisoindole-1,3(2*H*)-dione)] was prepared from nadic anhydride and MDA by a modification of literature procedures.[28] In turn, nadic anhydride was prepared via a Diels–Alder reaction of fresh cyclopentadiene with maleic anhydride. Cyclopentadiene was prepared via a reverse Diels–Alder reaction by refluxing DCPD at 180 °C. Cyclopentadiene was collected in an ice-cooled receiver and used for further reaction with maleic anhydride. The latter (4.00 g, 0.0408 mol) was first dissolved in ethyl acetate (15.0 mL) at room temperature under magnetic stirring. The solution was cooled for 15 min in an ice bath, and freshly prepared cyclopentadiene (4.0 mL) was added in the solution. The reaction mixture was stirred for another 20 min and 15.0 mL of hexane was added to complete precipitation of the crude product. The precipitate was separated by vacuum filtration and purified by recrystallization from ethyl acetate/hexane. Subsequently, nadic anhydride (1.656 g, 0.0101 mol) was dissolved in anhydrous NMP (15.0 mL) at room temperature under magnetic stirring. MDA (1.000 g, 0.005 mol) was added and the reaction mixture was stirred at room temperature for 24 h under N_2. At the end of the period, acetic anhydride (6.180 g, 0.0606 mol) and pyridine (1.0 mL) were added and the reaction mixture was heated at 100 °C for 6 h. The mixture was allowed to cool at room temperature, and the precipitate was washed with methanol, followed by drying under vacuum at 70 °C for 24 h. Yield: 2.0 g (75%); mp 243–245 °C (lit.[28a] mp 244 °C for the *endo,endo*- isomer). ^{1}H NMR (400 MHz, $CDCl_3$) δ 7.22 (d, J = 8.4 Hz, 4H), 7.05 (d, J = 8.4, 4H), 6.24 (t, J = 1.8, 4H), 3.98 (s, 2H), 3.49 (m, 4H), 3.41 (dd, J = 1.5 Hz, J = 2.9 Hz, 4H), 1.75 (dt, J = 1.6 Hz, J = 8.8 Hz, 2H), 1.58 (dt, J = 1.6 Hz, J = 8.8 Hz, 2H); ^{13}C NMR (100 MHz, $CDCl_3$) δ 176.78, 140.76, 134.49, 129.88, 129.56, 126.56, 52.13, 45.66, 45.38, 41.01; IR (KBr) 2990, 1770, 1710, 1510, 1380, 1180, 840, 745, 620 cm^{-1}. Elemental Analysis, (CHN % w/w). Found: C: 75.47; H: 5.04; N: 5.71. Theoretical: C: 75.92; H: 5.31; N: 5.71.

2.3. Synthesis of Polyimide Aerogels from bis-NAD via ROMP. Polyimide aerogels were prepared by mixing two solutions, one containing **bis-NAD** in NMP and one with moisture-tolerant Grubbs' catalyst **GC-II** in toluene. Different sets of samples with different bulk densities were obtained by varying the concentration of **bis-NAD**. Aerogel samples are abbreviated as **bis-NAD-xx**, where the extension -**xx** stands for the weight percentage of **bis-NAD** in the **bis-NAD** plus NMP mixture. All formulations are summarized in Table 1. Because **bis-NAD** has limited solubility in NMP at room temperature, heating at 60 °C was required in order to make the 2.5% and 5% w/w **bis-NAD** solutions, while the 10%, 15%, and 20% w/w **bis-NAD** solutions were heated at 90 °C. **GC-II** in 50 μL of toluene (see Table 1) was added to the **bis-NAD** solution, and the mixture was shaken vigorously and was poured into molds (Wheaton polypropylene OmniVials, Part No. 225402, 1 cm in diameter, or 15-cm^3 Fisherbrand Class B amber glass threaded vials, 1.8 cm in inner diameter, Part No. 03-339-23D; the latter molds were used for samples prepared for compression testing). All solutions gelled within 10–20 min, except the 20% w/w **bis-NAD** sol, which gelled within 1 min. The resulting wet gels were aged in their molds for 12 h at 90 °C, washed with NMP (4 washes, 8 h per wash), 1,4-dioxane (4 washes, 8 h per wash), acetone (4 washes, 8 h per wash), and dried in an autoclave with liquid CO_2 to yield **bis-NAD-xx** polyimide aerogels.

dx.doi.org/10.1021/cm200323e |*Chem. Mater.* 2011, 23, 2250–2261

2.4. Methods. Drying with liquid CO_2, taken out as a supercritical fluid (SCF), was conducted in an autoclave (SPI-DRY Jumbo Supercritical Point Dryer, SPI Supplies, Inc. West Chester, PA). Bulk densities (ρ_b) were calculated from the weight and the physical dimensions of the samples. Skeletal densities (ρ_s) were determined with helium pycnometry, using a Micromeritics AccuPyc II 1340 instrument. Porositiy (Π) values were determined from ρ_b and ρ_s values:

$$\Pi = 100 \times \left[\frac{(1/\rho_b) - (1/\rho_s)}{1/\rho_b}\right]$$

Surface areas and pore size distributions were measured by N_2 sorption porosimetry, using a Micromeritics ASAP 2020 surface area and porosity analyzer. Samples for surface area and skeletal density determination were outgassed for 24 h at 80 °C under vacuum before analysis. Average pore diameters were determined by the $4 \times V_{Total}/\sigma$ method, where V_{Total} is the total pore volume per gram of sample and σ, the surface area determined by the Brunauer−Emmett−Teller (BET) method. V_{Total} can be calculated either from the single highest volume of N_2 adsorbed along the adsorption isotherm or from the relationship $V_{Total} = (1/\rho_b) - (1/\rho_s)$. If the two average pore diameters coincide, it is taken as proof that the material lacks macroporosity. Liquid ^{1}H and ^{13}C NMR of **bis-NAD** were obtained with a 400 MHz Varian Unity Inova NMR instrument (100 MHz carbon frequency). Elemental analysis was conducted using a Perkin−Elmer elemental analyzer (Model 2400 CHN). Infrared (IR) spectra were obtained in KBr pellets, using a Nicolet-FTIR Model 750 spectrometer. Solid-state ^{13}C NMR spectra were obtained with samples ground into fine powders on a Bruker Avance 300 spectrometer with a carbon frequency of 75.475 MHz, using magic-angle spinning (at 7 kHz) with broadband proton suppression and the CPMAS TOSS pulse sequence for spin sideband suppression. Thermogravimetric analysis (TGA) was conducted under N_2 or air with a TA Instruments Model TGA Q50 thermogravimetric analyzer, using a heating rate of 10 °C min^{-1}. Scanning electron microscopy (SEM) was conducted with Au-coated samples on a Hitachi Model S-4700 field-emission microscope. The crystallinity of the polyimide samples was determined by X-ray diffraction (XRD) using a Scintag Model 2000 diffractometer with Cu Kα radiation and a proportional counter detector equipped with a flat graphite monochromator. The identity of the fundamental building blocks of the two materials was probed with small-angle neutron scattering (SANS), using ~2-mm-thick disks cut with a diamond saw from cylinders similar to those used for mechanical testing, on a time-of-flight, low-Q diffractometer (LQD) at the Manuel Lujan, Jr. Scattering Center of the Los Alamos National Laboratory.[29] The scattering data are reported in the absolute units of differential cross section per unit volume (cm^{-1}), as a function of Q, the momentum transferred during a scattering event. Quasi-static mechanical testing under compression was conducted on an Instron Model 4469 universal testing machine frame, following the testing procedures and specimen length-to-diameter ratio (2.0 cm/1.0 cm) that was specified in ASTM D1621-04a ("Standard Test Method for Compressive Properties of Rigid Cellular Plastics"). The recorded force, as a function of displacement (machine-compliance corrected), was converted to stress as a function of strain. The thermal diffusivity (R) of the **bis-NAD-xx** aerogels was measured at 23 °C with a Netzsch NanoFlash Model LFA 447 Flash diffusivity instrument, using disk samples ~1 cm in diameter, 2.0−2.2 mm thick (the thickness of each sample was measured with 0.01 mm resolution and was entered as required by the data analysis software). Heat capacities at 23 °C of powders of the same samples (4−8 mg), needed for the determination of their thermal conductivity, λ, were measured using a TA Instruments Differential Scanning Calorimeter Model Q2000 calibrated against a sapphire standard and run from −10 to 40 °C at 0.5 °C min^{-1} in the modulated T4P mode, using 60 s modulation period and 1 °C as modulation amplitude. The raw data with **bis-NAD-xx** were multiplied by the calibration factor (0.920 ± 0.028) determined with rutile, KCl, Al, graphite, and corundum just before our experiments.

3. RESULTS AND DISCUSSION

3.1. Synthesis and Characterization of bis-NAD. The monomer, **bis-NAD**, was prepared in high yield (75%) via the DuPont route from nadic anhydride and 4,4′-methylenedianiline (MDA) via chemical dehydration of the intermediate diamic acid (see Scheme 1) and was characterized by elemental analysis, infrared (IR) spectroscopy, ^{1}H nuclear magnetic resonance (NMR), and ^{13}C NMR. The IR spectrum (Figure 1) is dominated by the imide C═O symmetric and asymmetric stretches at 1710 and 1770 cm^{-1}, respectively, and by the C−N stretch at 1380 cm^{-1}. The absorption at 1510 cm^{-1} is assigned to the C═C stretch, while the absorption at 1170 cm^{-1} is attributed to the ═C−H in-plane bending from both the nadic and aromatic rings. In ^{13}C NMR (Figure 2, peak assignment by simulation), all carbons of **bis-NAD** are resolved. No impurities are visible, which is consistent with the elemental analysis data (see the Experimental Section). The resonance at 177 ppm is assigned to the imide carbonyl, the one at 134 ppm is assigned to the sp^2-carbons of the norbornene moieties, and the several resonances between 125 and 145 ppm are assigned to the aromatic carbons. The peak at 41 ppm is due the $-CH_2-$ group of MDA, while the peaks between 43 and 55 ppm are assigned to the aliphatic carbons of the norbornene end-caps. Using thermogravimetric analysis (TGA) (Figure 3A), **bis-NAD** is shown to be thermally stable,

Scheme 1. Synthesis of bis-NAD

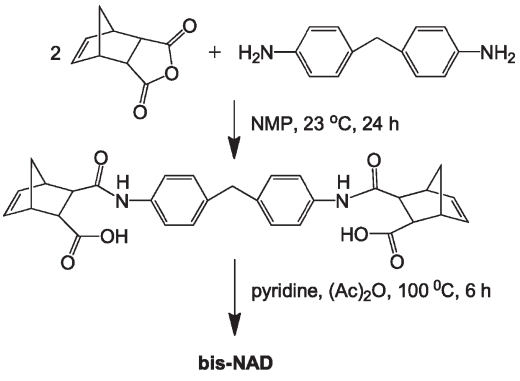

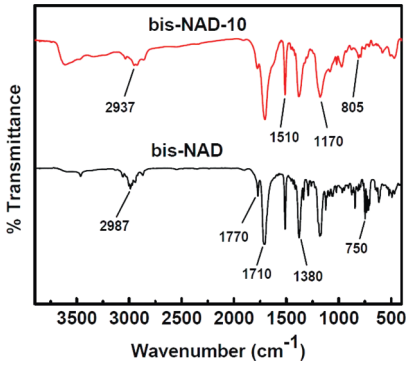

Figure 1. Infrared (IR) data for **bis-NAD** monomer and a representative ROMP-derived polyimide aerogel.

dx.doi.org/10.1021/cm200323e |*Chem. Mater.* 2011, 23, 2250–2261

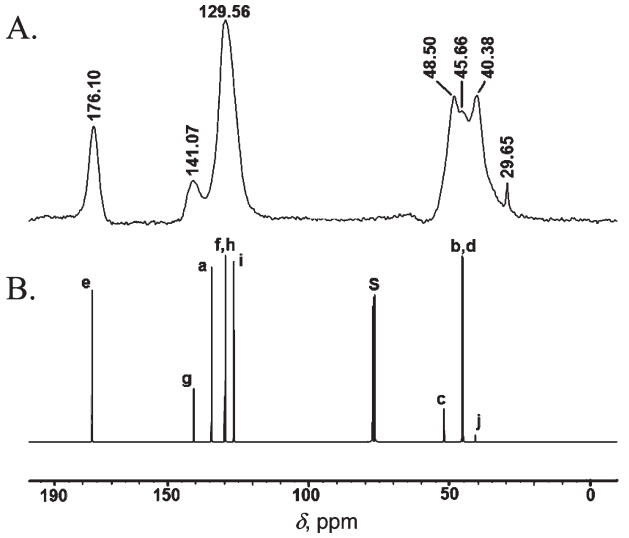

Figure 2. (A) Representative CPMAS ^{13}C NMR spectrum of a ROMP-derived polyimide aerogel (case shown: **bis-NAD-10**). The resonance at 29.65 ppm is attributed to residual solvent (acetone). (B) Liquid ^{13}C NMR of the **bis-NAD** monomer in $CDCl_3$ (marked "S"). For peak assignments, see the structure described in the text.

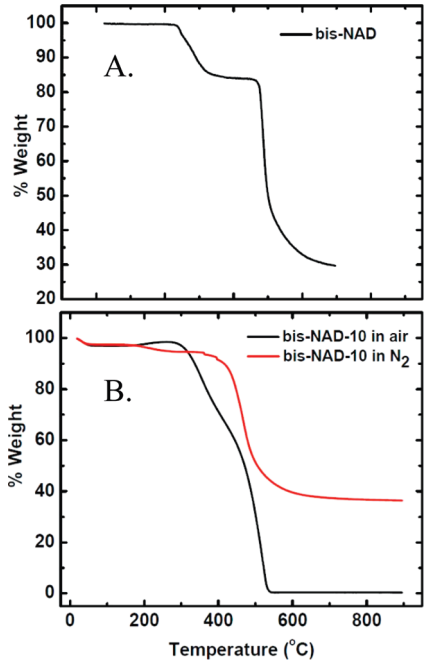

Figure 3. (A) Thermogravimetric analysis (TGA) data for the monomer (**bis-NAD**) at 10 °C min^{-1}. (B) TGA data for a representative ROMP-derived polyimide sample, as shown at the same heating rate.

up to ~220 °C, undergoing a 16% mass loss between 220 °C and 350 °C, because of a reverse Diels–Alder reaction (loss of cyclopentadiene was confirmed by mass spectrometry). The observed mass loss corresponds to a loss of one end-cap per **bis-NAD** molecule (see Scheme 2), which, in turn, may imply that the newly created maleimide reacts with the norbornene end-cap of another molecule to a more stable adduct. This matter was not investigated further; however, the TGA data of Figure 3A

Scheme 2. Primary Thermal Decomposition Mechanism of bis-NAD

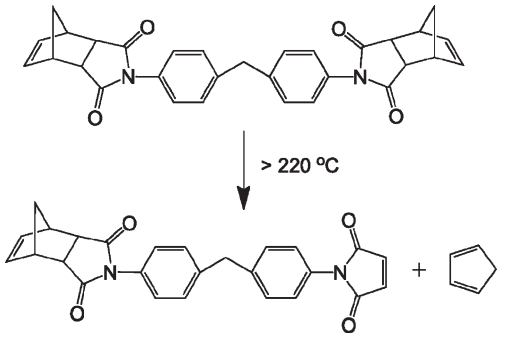

become important in assessing whether all norbornene end-caps react during the ROMP gelation process, as discussed below.

3.2. Synthesis of bis-NAD-xx Polyimide Aerogels. **Bis-NAD**-related molecules (e.g., with 4,4′-dioxyaniline bridges) have been cross-linked before thermally or with microwaves.[30] Cross-linking of **bis-NAD** itself via ROMP is summarized in Scheme 3. Monoliths with different densities were obtained by varying the monomer concentration. The amount of the **GC-II** catalyst was varied inversely to the monomer concentration, in order to keep the gelation time under 20 min. Wet gels were aged in their molds for 12 h at 90 °C to ensure that all monomer is consumed and incorporated in the gels.[31] This was confirmed in two ways: first, by analyzing the washes for unreacted monomer, and second by the mass balance between the aerogels and the amount of **bis-NAD** used for their preparation. Nevertheless, aging has not been optimized time-wise. Wet gels were solvent-exchanged from NMP, through 1,4-dioxane, to acetone before they were dried with liquid CO_2 taken out superscritically at the end. Right after gelation, wet gels are yellowish-brown; they look off-white after NMP washes, because of remaining traces of the catalyst, and completely white after treatment with 1,4-dioxane and acetone. Dry aerogels were opaque-white (see photograph in Scheme 3).

3.3. Characterization of bis-NAD-xx Aerogels. *3.3.a. Chemical Characterization.* The polymerization of **bis-NAD** proceeds according to Scheme 4. ROMP does not alter the identity of the functional groups, and elemental analysis of **bis-NAD-xx** gives results similar to those for the monomer (%w/w: C, 73.99; H, 5.21; N, 5.61; versus C, 75.47; H, 5.04; N, 5.71 for the monomer). Similarly, in IR (Figure 1) analysis, the most prominent differences between **bis-NAD** and **bis-NAD-xx** are associated with the CH_2 and CH stretches that move to lower frequencies after ring opening of the nadimide (from the 2987–2871 cm^{-1} range to the 2937–2855 cm^{-1} range), and an increase from 750 cm^{-1} to 805 cm^{-1} in the absorption frequency of the =C–H out-of-plane bending. In CPMAS ^{13}C NMR of **bis-NAD-xx**, after ring opening, the alkene carbon resonance moves upfield (from 134 ppm originally), merging with the aromatic carbons. The resonance of the bridgehead carbon (labeled as "c") moves also upfield from 52 to the 30–42 ppm range, merging with the MDA methylene bridge (Figure 2). After ring opening, the "b" and "d" aliphatic carbons of the norbornene ring move slightly downfield, from 45.66 ppm to 48.50 ppm and from 45.38 ppm to 45.66 ppm, respectively. Those spectroscopic changes, however, do not warrant that all norbornene moieties have been cross-linked. TGA of **bis-NAD-xx**

dx.doi.org/10.1021/cm200323e |*Chem. Mater.* 2011, 23, 2250–2261

Scheme 3. Flowchart for the Preparation of Polyimide Aerogels from bis-NAD

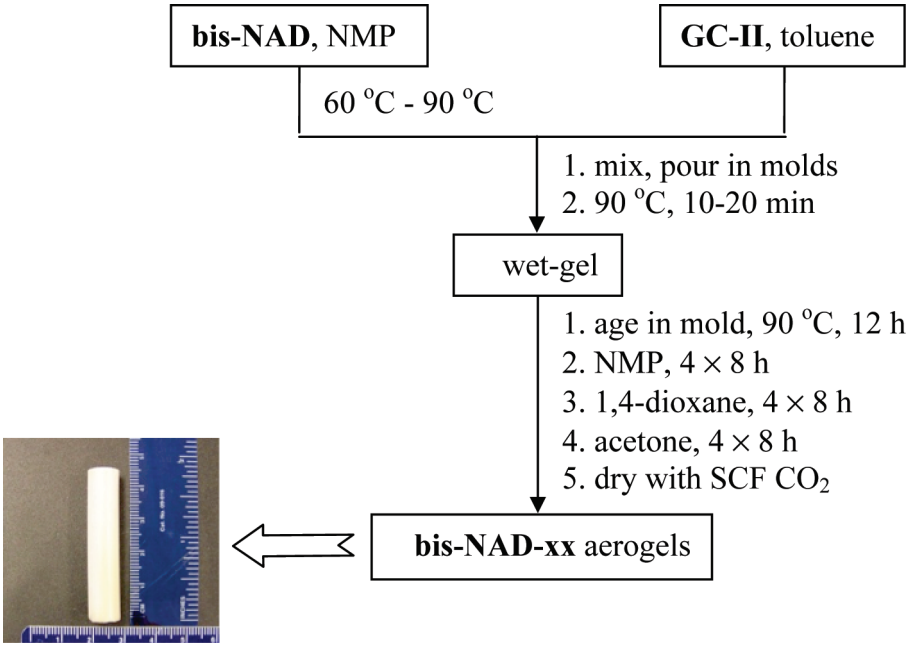

Scheme 4. Polymerization of bis-NAD via ROMP

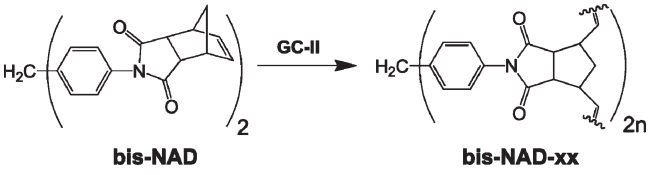

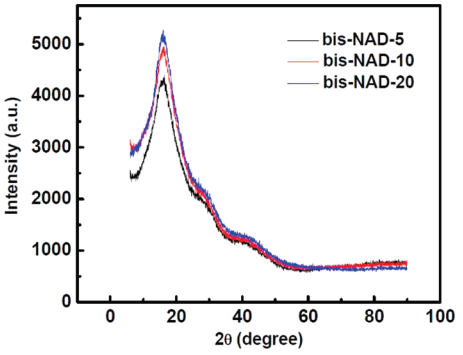

Figure 4. X-ray diffraction (XRD) spectra of three representative ROMP-derived polyimide aerogels (as shown).

in N_2 (see Figure 3B) shows a small initial mass loss (~3%) below 100 °C (attributable to residual solvents), and a second small mass loss (~3%) in the 190−240 °C range consistent with a reverse Diels−Alder reaction of a small amount of dangling unreacted norbornene moieties, according to Scheme 2. These moieties may become inaccessible to the catalyst in a closely packed polymer. In that regard, XRD shows that all samples have a high degree of crystallinity (up to 53%; see Figure 4), suggesting a regular packing of the polymer chains within the fundamental building blocks of the skeletal framework. This, in turn, implies early phase separation of a polymer with substantial linearity.

3.3.b. Microstructural Characterization. Porosity and pore structure are reported as a function of the bulk density (ρ_b), which, in turn, is related to the monomer concentration in the sol. Results are summarized in Table 2. The morphology of the pore walls (i.e., the skeletal framework) was inspected via scanning electron microscopy (SEM) and their composition was investigated at the fundamental building block level with SANS.

Although all **bis-NAD** is incorporated in the final aerogels, ρ_b does not vary linearly with the concentration of the monomer in the sol: e.g., the ρ_b value of **bis-NAD-20** is 0.660 g cm^{-3} but that of **bis-NAD-2.5** is 0.134 g cm^{-3}, not 8 times less as expected from the relative concentrations of the monomer. This is because all samples shrink in reverse order to the concentration of **bis-NAD** in the sol: **bis-NAD-2.5** samples shrink 39%, relative to the molds, while **bis-NAD-20** samples shrink less (28%; see Table 2). Minimal shrinking (1−3% in linear dimensions) is observed during gelation and aging (syneresis), no further shrinkage takes place during NMP and 1,4-dioxane washes, while the majority of shrinkage is observed during the final acetone washes. No shrinking is observed during SCF drying. Therefore, exhibiting typical gel-like semipermeable membrane behavior, **bis-NAD-xx** wet gels swell until the pressure created by stretching of the framework -which, therefore, must be quite flexible- is balanced by the osmotic pressure of the internal "solution."[32] Thus, changing the polarity of the solvent changes the degree of swelling. Interparticle covalent bonding is more prevalent in higher-density samples; hence, they stretch less, swell less, and, therefore, shrink less.

All skeletal density (ρ_s) values fall in the 1.26−1.36 g cm^{-3} range, the variation is significant, but since there is no systematic trend with the monomer concentration, it is rather attributed to random error. Porosity (Π) values, which are calculated from the ρ_b and ρ_s values, decrease from 90% to 48% as the bulk density

dx.doi.org/10.1021/cm200323e |*Chem. Mater.* 2011, 23, 2250–2261

Table 2. Selected Properties of Polyimide Aerogels via ROMP

sample	diameter (cm)[a]	shrinkage (%)[a,b]	bulk density, ρ_b (g cm^{-3})[a]	skeletal density, ρ_s (g cm^{-3})[c]	porosity Π (% void space)	surface area, (m^2 g^{-1})[d]	average pore diameter (nm)[e]	average pore diameter (nm)[f]
bis-NAD-2.5	0.609 ± 0.005	39 ± 1	0.134 ± 0.002	1.360 ± 0.014	90.1	632 [180]	13.8 [42.6]	33.4 [69.7]
bis-NAD-5	0.639 ± 0.005	36 ± 1	0.261 ± 0.005	1.325 ± 0.008	80.3	524 [124]	16.7 [23.5]	42.8 [67.6]
bis-NAD-10	0.685 ± 0.005	32 ± 1	0.341 ± 0.011	1.260 ± 0.003	72.9	438 [72]	16.4 [19.6]	42.6 [44.2]
bis-NAD-15	0.705 ± 0.007	30 ± 1	0.507 ± 0.014	1.292 ± 0.004	60.7	298 [29]	14.8 [16.1]	30.7 [12.8]
bis-NAD-20	0.725 ± 0.005	28 ± 1	0.660 ± 0.019	1.260 ± 0.002	47.6	210 [19]	12.9 [13.7]	20.4 [5.0]

[a] Average of three samples. (Mold diameter: 1.0 cm). [b] Shrinkage =100 × (sample diameter − mold diameter)/(mold diameter). [c] Single sample, average of 50 measurements. [d] BET surface area of the micropore (by *t*-plot, using the Harkins and Jura method). [e] By the $4 \times V_{Total}/\sigma$ method. For the first number, V_{Total} was calculated by the single-point adsorption method; for the number in brackets, V_{Total} was calculated via $V_{Total} = (1/\rho_b) - (1/\rho_s)$. [f] From the BJH desorption plot. First numbers are the peak maxima; numbers in brackets are the widths at half maxima.

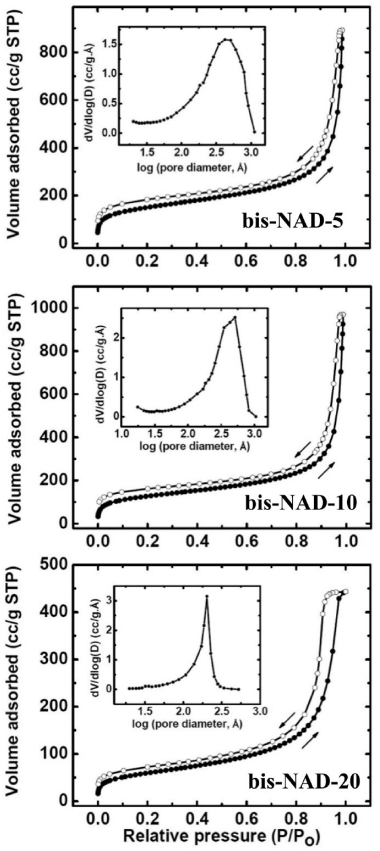

Figure 5. N_2 sorption isotherms for the **bis-NAD-xx** aerogels, as a function of the bulk density (ρ_b). Insets show BJH desorption plots. Data are summarized in Table 2.

increases (see Table 2). N_2-sorption porosimetry (Figure 5) suggests that the most dense samples are strictly mesoporous. Specifically, at lower densities (≤0.34 g cm^{-3}), the N_2 absorption isotherms rise above a value of P/P_0 = 0.9 and do not reach a well-defined saturation plateau, indicating that a significant portion of the porosity is due to macropores (defined as pores with diameters of >50 nm); on the other hand, the same isotherms do show narrow hysteresis, which is an indication of some mesoporosity. As the bulk density increases (≥0.5 g cm^{-3}) the onset of the quick rise in the volume of N_2 adsorbed moves to lower P/P_0 values (to $P/P_0 \approx 0.8$), the isotherms reach saturation and they show large H2-type hysteresis loops, all of which is consistent with mostly mesoporous materials and "ink bottle"-type pores.[33] Quantitatively, average pore diameters calculated by the $4 \times V_{Total}/\sigma$ method, using V_{Total} either from the maximum volume adsorbed from the isotherms (captures mesopores), or from $V_{Total} = (1/\rho_b) - (1/\rho_s)$ (captures all pores) diverge significantly at lower densities (signifying macroporosity), but converge for the denser samples (signifying mesoporosity; see Table 2). Similarly, BJH-desorption plots (shown as insets in Figure 5) give broad (with hints for bimodal) pore-size distributions for the lower density samples, but they are quite narrow and monomodal at higher densities. (It is noted that, although BJH maxima are also summarized in Table 2, they should not be considered quantitatively, because all adsorption−desorption isotherms are consistently open-looped, indicating swelling of nonrigid pores[33,34] in agreement with conclusions reached above from shrinkage data.) At the low P/P_0 end of the isotherms, the significant quick rise of the volume of N_2 adsorbed indicates the presence of a significant fraction of micropores. Data analysis within the range of $0.05 < P/P_0 < 0.3$, according to the BET model (Table 2), shows that, at low densities, the surface area is quite high (up to 632 m^2 g^{-1} for **bis-NAD-2.5**), decreasing (but remaining quite significant) to 210 m^2 g^{-1} at ρ_b = 0.660 g cm^{-3} (**bis-NAD-20** samples). *t*-Plot analysis of the isotherms within the range of $0.05 < P/P_0 < 0.5$, using the Harkins and Jura method,[35] shows that, at low densities, up to 35% of the surface area comes from micropores, decreasing to <10% in the denser samples (**bis-NAD-15** and **bis-NAD-20**).

SEM analysis (Figure 6) shows that all of the samples consist of particles that are agglomerating together to form larger clusters. Lower-density samples (<0.5 g cm^{-3}) show clearly the presence of macropores, which is consistent with the N_2-sorption analysis above. The minimum particle diameter observed by SEM (~20 nm) is rather uniform throughout all densities. Those smallest particles assemble to larger aggregates (50−100 nm in diameter), but they are best defined (discernible) in the lowest and highest density samples (**bis-NAD-5** and bis-**NAD-20**, respectively). The medium density samples (**bis-NAD-10**) are fuzzier and the smallest particles look as if they are fused together into larger clusters. The smallest particles in the highest density samples (**bis-NAD-20**) are dispersed rather uniformly in space, rendering identification of the larger aggregates difficult. A quantitative assessment of the makeup of the skeletal framework was obtained with SANS; the data are included in Figure 6. In addition, the results obtained by applying the Beaucage Unified Model analysis,[36] which models the samples as having multiple levels of structure, each with a distinct characteristic length, corresponding hierarchically (starting from high *Q* values) to a particle, aggregate, and agglomerate, are summarized in

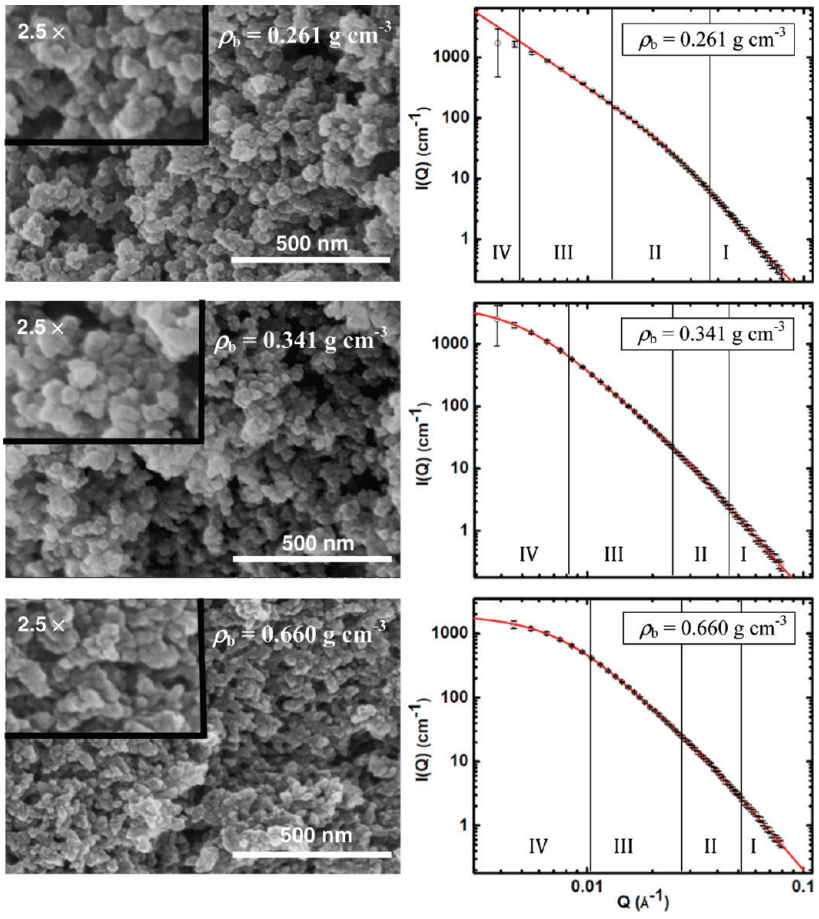

Figure 6. Scanning electron microscopy (SEM) and small-angle neutron scattering (SANS) analyses of ROMP-derived **bis-NAD-xx** aerogels, as a function of the bulk density (ρ_b). Refer to Table 3 for information from the SANS data and for the meaning of Regions I–IV .

Table 3. Small-Angle Neutron Scattering (SANS) Data for Polyimide Aerogels via ROMP (Footnoted Terms Refer to Figure 6)

	Primary Particles		Secondary Particles		
sample	Porod shape[a]	R_G (nm)[b] []^c	R_G (nm)[d] []^c	D_m[e]	D_S[e]
bis-NAD-5	4.0 ± 0.1	6.3 ± 1.1 [16.4]	*f*	2.34 ± 0.03	
bis-NAD-10	4.0 ± 0.1	6.5 ± 1.2 [16.9]	32.8 ± 2.5 [85.2]		2.9 ± 0.1
bis-NAD-20	4.0 ± 0.1	6.1 ± 1.7 [15.8]	23.1 ± 1.1 [60]		3.0 ± 0.5

[a] From Region I. [b] From Region II. [c] The value in brackets represents the particle diameter, which is defined as $2R$, where R is the particle radius. The radius of gyration is given as $R_G = 0.77R$. [d] From Region IV. [e] From Region III. [f] Region IV in this sample was beyond the experimentally accessible range of the scattering vector Q; thus, R_G could not be estimated.

Table 3. Furthermore, the Unified Model allows analysis of such hierarchical structures over the full range of Q, the momentum transferred in a scattering event, allowing deconvolution of overlapping length scales that can lead to subtle changes in the data, such as a change in slope. Over all densities and the entire range of the scattering Q, SANS shows two Guinier regions (knees), which are indicative of characteristic length scales and two power-law regions (which appear to be linear on the log–log plots in Figure 6). Plots of the SANS data found in Figure 6 have been divided into four regions (in Q), for ease of identifying the different structural levels. The Unified Model provides the radii of gyration (R_G) from the Guinier knees (Regions II and IV in the data of Figure 6) and the fractal dimensions of the secondary particles from the linear region (Region III).

The slope of the data in Region I provides information about the surface characteristics of the primary particles themselves. Matching and comparing the SANS data of Table 3 with the SEM data of Figure 6 identifies the minimum SEM particles as polydisperse, but monomodal primary particles, 16–17 nm in diameter, with smooth (nonfractal) interfaces (the slopes in Region I are all uniformly equal to 4.0). The size of the primary particles does not change with density (i.e., the concentration of **bis-NAD** in the sol), in analogy to silica.[37] Secondary aggregates are larger for medium-density samples (85.2 nm in diameter for **bis-NAD-10**), but their size decreases as the density increases (60 nm for **bis-NAD-20**). Guinier Region IV for **bis-NAD-5** was located at the edge of the accessible Q-range and the secondary particle size could not be

measured. Nevertheless, in those lower-bulk-density samples, primary particles assemble into the secondary aggregates fractally (mass fractal dimension, $D_m = 2.34 \pm 0.03$), which suggests diffusion-limited aggregation as the growth mechanism.[38] As the bulk density increases (**bis-NAD-10** and **bis-NAD-20** samples), the Region III exponent increases and falls at the limit between mass and surface fractals. The level of uncertainty associated with the large size of both the primary and secondary particles causes significant overlap of Guinier Regions II and IV with the linear Region III, from which the fractal dimension is estimated, making assessment by SANS alone inconclusive. However, combining the SANS and SEM results suggests that we are dealing with surface fractals of nonfractal objects. With the Region III slope being attributed to surface fractals with $D_S = 3.0$, secondary particles of **bis-NAD-10** and **bis-NAD-20** are then classified as surface fractal closed-packed objects. Transition from the more-open fractal structure to the more-dense nonfractal one justifies the decrease in the percentage of micropore surface area, from 35% in the lower-density samples to <10% in the higher-density samples.

Considering the XRD and SANS data together—namely, the closed packing of the polymeric strands implied by XRD and the invariance of the primary particle size revealed by SANS—supports fast polymerization to mostly linear oligomers that always reach their solubility limit at the same point, irrespective of the concentration of **bis-NAD** in the sol, and become phase-separated into uniform-sized primary particles, which are surface-active through dangling norbornene moieties, or catalyst-terminated polymer strands. At the lowest concentrations (e.g., **bis-NAD-5** samples), primary particles react with each other via a diffusion-limited mechanism to form fractal secondary particles that, in turn, form a gel. Values of $D_S = 3.0$ at higher concentrations (e.g., **bis-NAD-10** and **bis-NAD-20** samples) might be associated with fast ROMP, which fills the sol with primary particles that react with their next neighbor through a bond percolation model, yielding non(mass) fractal secondary objects.[39] Cross-linking of the polymer strands most probably continues throughout those gel-forming processes. In the case of the **bis-NAD-20** samples, extremely fast ROMP consumes all monomer quickly (recall, for example, that gelation occurs within <1 min in those samples). Somewhat slower ROMP in the more-dilute **bis-NAD-10** samples is followed by the accumulation of monomer on the secondary particles (a monomer-cluster-growth-like process), which explains the fuzziness in SEM observation.

3.3.c. Application-Related Bulk Properties. Polyimides are thermally stable polymers; therefore, appropriate applications for **bis-NAD-xx** aerogels include high-temperature thermal and acoustic insulation. Relevant properties to monitor include thermal stability, mechanical strength, and thermal conductivity.

Thermal Stability. Despite their resemblance to PMR-type polyimides (both materials are prepared from the same norbornene end-capped oligomers),[24] ROMP-derived **bis-NAD-xx** aerogels have unsaturated backbones (see Scheme 4). Therefore, their use in air might be problematic. Indeed, TGA (see Figure 3B) of **bis-NAD-xx** shows a mass increase above ~200 °C, presumably by reaction with oxygen. PMR-type polyimides are rated for operation up to 10 000 h at 290 °C,[24] which is obviously not possible with as-prepared **bis-NAD-xx**. Increasing the molecular weight of the monomer, or post-gelation saturation of the double bonds might be approaches around this issue. Conveniently, that process could be coupled with increasing the hydrophobicity and reducing the flammability of the material.

Mechanical Properties. As stated in the Introduction, organic aerogels are pursued partly as alternatives to polymer cross-

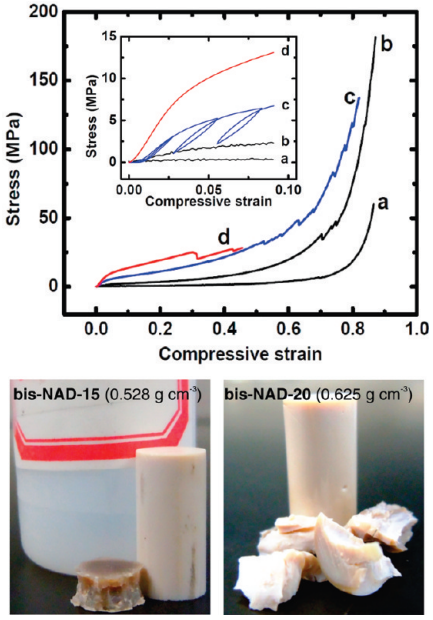

Figure 7. Top: Stress−strain curves under quasi-static compression of the **bis-NAD-xx** aerogels, as a function of the bulk density (**bis-NAD-5**, $\rho_b = 0.24$ g cm^{-3} (curve a); **bis-NAD-10**, $\rho_b = 0.39$ g cm^{-3} (curve b); **bis-NAD-15**, $\rho_b = 0.53$ g cm^{-3} (curve c); and **bis-NAD-5**, $\rho_b = 0.63$ g cm^{-3} (curve d)). Inset shows a magnification of the early, almost-elastic region, including loading−unloading data for a **bis-NAD-15** sample. Bottom of the figure shows photographs of two samples as indicated, before and after compression, showing the different modes of failure.

Table 4. Mechanical Characterization Data under Quasi-static Compression of Polyimide Aerogels[a]

sample	bulk density, ρ_b (g cm^{-3})	strain rate (s^{-1})	Young's modulus, E (MPa)	speed of sound (m s^{-1})	yield stress at 0.2% offset strain (MPa)	ultimate strength, UCS (MPa)	ultimate strain (%)	Poisson's ratio	Specific Energy, abs (J g^{-1})	Specific Energy, abs (J cm^{-3})[b]
bis-NAD-5	0.240	0.035	NA	NA	0.36 ± 0.02	45.0 ± 21.6	85.1 ± 2.1	0.267 ± 0.037	16.7 ± 3.9	4
bis-NAD-10	0.390	0.035	48 ± 8	350.8	2.25 ± 0.12	168.4 ± 18.6	88.1 ± 1.6	0.269 ± 0.041	50.2 ± 2.4	20
bis-NAD-15	0.528	0.035	173 ± 13	572.4	6.05 ± 0.17	127.4 ± 14.1	79.6 ± 3.1	0.286 ± 0.006	50.1 ± 2.0	27
bis-NAD-20	0.625	0.035	288 ± 0.5	678.7	11.2 ± 0.079	27.7 ± 0.8	40.6 ± 6.8	0.299 ± 0.008	14.7 ± 1.6	9

[a] Average of two samples. [b] Per unit volume energy absorption, calculated from the energy absorption per unit mass multiplied by bulk density.

dx.doi.org/10.1021/cm200323e |*Chem. Mater.* 2011, 23, 2250–2261

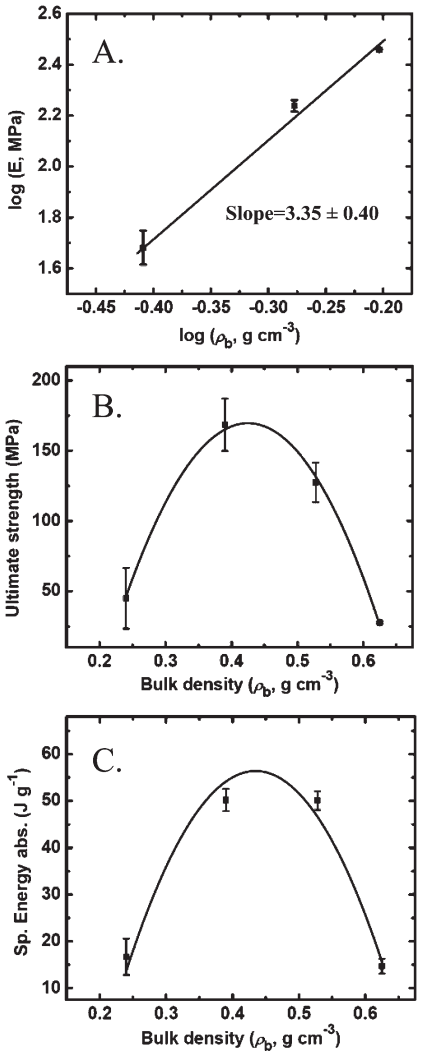

Figure 8. (A) Log−log plot of the Young's modulus versus bulk density of various **bis-NAD-xx** aerogels. (B, C) Variation of the ultimate compressive strength (panel B) and energy absorption (panel C) of the same **bis-NAD-xx** aerogels, each as a function of their bulk density. (Lines have been added to guide the eye.)

linked silica aerogels for their facile one-step synthesis and for their mechanical properties. In that regard, ROMP-derived polyimides were investigated under quasi-static compression. The stress−strain curves (Figure 7) show very short, almost-elastic ranges up to ~3% strain, followed by plastic deformation and hardening up to 70% strain, because of pore collapse. The fact that the early part of the stress−strain curves is almost elastic was confirmed by conducting loading and unloading tests (Figure 7, inset); it was found that the unloading curve after loading to 3% strain almost follows the loading curve with 0.2% remaining strain. (By comparison, loading up to 5.5% strain results in 2% unrecovered strain, and loading up to 8% strain gives 4% unrecovered strain.) Interestingly, after reaching the 0.2% offset yield stress, which is a conventional measure of the incipient of plastic deformation, the stress continues to increase with strain. This phenomenon is different from plastic foams[40] in which, after reaching the yield strength, the stress−strain curve shows a plateau associated with the collapse of pores, because of cell-wall buckling. It is likely that the small ratio of pore size to wall thickness (refer to SEM) prevents pore walls from buckling during compression of the sample. As a result, hardening at strains prior to 70% are attributed to nanobending deformations.

Macroscopically, in no case do the samples buckle during compression, and all Poisson's ratios are in the range of 0.27−0.30, reflecting little lateral expansion, unless during the late stages of the test, when pores have been substantially closed and samples start to expand radially. Ultimately, lower-density samples ($\leq$0.5 g cm^{-3}) undergo compressive failure at >80% strain, but the most dense samples (**bis-NAD-20**, ρ_b = 0.6 g cm^{-3}) fail catastrophically by fragmentation at much lower strains (~40%, see Figure 7). The ultimate compressive strains roughly follow the corresponding porosities of the samples (compare Tables 2 and 4). The Young's modulus (E, calculated from the slope of the early linearly elastic range), the speed of sound (calculated from the Young's modulus and the bulk density via $(E/\rho_b)^{0.5}$), and the yield stress at 0.2% offset strain all increase as the bulk density increases. Specifically, the Young's modulus follows a power law relationship with bulk density (Figure 8A) of the type $E \approx (\rho_b)^{3.35}$. The sensitivity (exponent) is higher than that observed with native silica aerogels (~3.0),[41] cross-linked silica aerogels (3.10),[42] cross-linked vanadia aerogels (1.87),[41c] and polyurea organic aerogels,[43] signifying the vastly different nature of the interparticle bridging: in **bis-NAD-xx**, the neck zones are purely polymeric, whereas in polymer-cross-linked aerogels, they are mixed organic−inorganic. On the other hand, the ultimate strength, as well as the ability for the material to store energy (referenced as toughness and quantified by the integral of the stress−strain curve) vary nonmonotonically with density: as shown in Figures 8B and 8C, they both increase with density in the beginning, then they reach a maximum, and, afterward, they decline. That decline in strength and toughness coincides with both the change in the failure mode (see photographs in Figure 7) and the decline in the ultimate strain at failure (see data in Table 4).

A monotonic variation of the Young's modulus with density and a simultaneous nonmonotonic variation of the ultimate strength and toughness (see Figure 8) also have been observed with polymer cross-linked silica aerogels, and that behavior is independent of the cross-linking polymer.[44,45] In those materials, the reinforcing polymeric tethers are placed on a preformed inorganic framework, and while all accumulated polymer contributes to stiffness,[46] only the bridging tethers between the nanoparticles contribute to strength and toughness.[44,45] In agreement with conclusions reached with silica aerogels,[47] changes in the fractal dimension (and, therefore, the connectivity within secondary particles) should not be relevant to the decline of the strength and toughness as the density increases. Indeed, the higher connectivity within the secondary particles of **bis-NAD-10** and **bis-NAD-20**, as indicated by their fractal dimension (Table 3), is not associated with an identifiable trend in their mechanical properties (see Table 4). Therefore, the trends in Figure 8 should be traceable to the intersecondary particle connectivity. Based on the microscopic characterization data, it was concluded that the growth mechanism of medium-density **bis-NAD-xx** samples is reminiscent of the cross-linking process of silica aerogels, in that gelation is followed by a monomer-cluster growth process, where particles continue to grow in size via continual reaction with the remaining monomer. That reinforces the intersecondary particle necks (in a cross-linked aerogel fashion), yielding stronger materials. At even higher monomer concentrations, reactions proceed fast, consuming all

Table 5. Thermal Conductivity Data for Selected bis-NAD-xx Samples [a]

sample	bulk density, ρ_b (g cm^{-3})	heat capacity, c_p (J g^{-1} K^{-1}) [b]	thermal diffusivity, R (mm^2 s^{-1}) [b]	thermal conductivity, λ (W m^{-1} K^{-1}) [b]
bis-NAD-10	0.338 ± 0.003	0.995 ± 0.030	0.091 ± 0.005	0.031 ± 0.00$_1$
bis-NAD-15	0.568 ± 0.003	1.088 ± 0.033	0.085 ± 0.001	0.053 ± 0.00$_2$
bis-NAD-20	0.622 ± 0.002	1.062 ± 0.032	0.096 ± 0.004	0.063 ± 0.00$_3$

[a] Average of three samples. [b] At 23 °C.

of the monomer quickly, and yield smaller particles with weaker interparticle necks, leading to a decline in ultimate strain and a concomitant decrease in ultimate strength and energy absorption.

Overall, at their best (i.e., at the medium density range), **bis-NAD-10** and **bis-NAD-15** aerogels compete favorably with (and, in many aspects, they are better than) polymer cross-linked silica aerogels. For example, polyurea cross-linked silica at ρ_b = 0.304 g cm^{-3}, process-optimized by statistical design of experiments (DoE) methods, are 77% porous with σ = 147 m^2 g^{-1}, a Young's modulus of 32 MPa, a yield stress at a 0.2% offset strain of 1.12 MPa, and an ultimate strength of 237 MPa.[45] By comparison, **bis-NAD-10** samples (ρ_b = 0.341 g cm^{-3}) are 73% porous, with σ = 438 m^2 g^{-1} (Table 2), a Young's modulus of 48 MPa, a yield stress at a 0.2% offset strain of 2.25 MPa, and an ultimate strength of 168 MPa, and they can absorb up to 50 J g^{-1} of energy (see Table 4). The latter figure renders them better than strong materials typically used for ballistic protection, such as 4130 steel (15 J g^{-1} at 7.84 g cm^{-3}), Kevlar-49 epoxy composites (11 J g^{-1} at 1.04 g cm^{-3}), and SiC ceramics (20 J g^{-1} at 3.02 g cm^{-3}).[48] Now, from an engineering design perspective, a fair comparison with standard materials should also extend from energy absorption per unit mass (J g^{-1}) to energy absorption per unit volume (J cm^{-3}). Using the latter metric, steel and SiC (117.6 J cm^{-3} and 60.4 J cm^{-3}, respectively) remain superior to **bis-NAD-xx** aerogels (27 J cm^{-3} at their best; see Table 4), but the latter still surpass Kevlar-49 fiber-epoxy composites (11.4 J cm^{-3}). However, since fiber-epoxy composites are rapidly replacing steel and ceramics in armor,[49] it is concluded that the additional volume requirement for absorbing a fixed amount of energy by Kevlar composites is easily taken into account in practice. Therefore, by and large, **bis-NAD-xx** aerogels are reasonable and, in fact, better alternatives.

Thermal Conductivity (λ). This was calculated from the thermal diffusivity (R) and the heat capacity (c_p) of **bis-NAD-xx** disks ~2.0 mm thick, using eq 1. The thermal diffusivity,

$$\lambda = \rho_b \times c_p \times R \qquad (1)$$

was measured using a flash method (see the Experimental Section),[50] where the sample is heated from one side and the temperature rise is observed as a function of time on the other side. Coating the samples on both sides with gold and carbon ensures absorption of the heat pulse and minimizes radiative pathways and pulse "bleed through."[51] Typical data are shown in Figure 9. The data analysis software employs the pulse-corrected Cowan model[52] to approximate the heat-transfer equation, using an initial value for the thermal diffusivity estimated by the time it takes for the detector voltage to reach its half-maximum value (marked as t_{50} in Figure 9). Subsequently, a least-squares fit is iteratively performed in a defined time range ($10 \times t_{50}$), and the value for thermal diffusivity, R, is obtained. (A value of 10 times t_{50} has been determined to be a suitable measure of the initial cooling event after the heat pulse.) Table 5 summarizes the data.

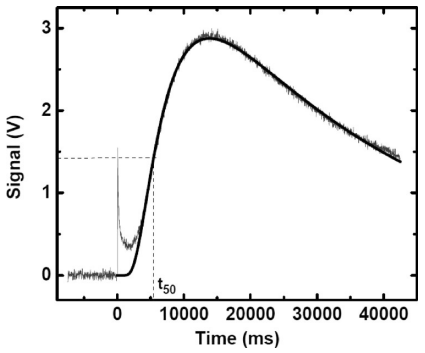

Figure 9. Temperature rise curve of the back face of a **bis-NAD-15** aerogel disk (9.32 mm in diameter, 2.17 mm thick, ρ_b = 0.568 g cm^{-3}) coated with gold and carbon on both faces, following a heat pulse incident to the front face. Dashed reference lines indicate t_{50}, which is the time required for the detector voltage (proportional to temperature) to reach half its maximum value. Data have been fitted to the pulse-corrected Cowan model (see text).

Because of the small variation of the thermal diffusivity with density and the constant value of the heat capacity, thermal conductivity scales linearly with the bulk density within the limits investigated and expresses the contribution of the through-lattice heat transfer. The thermal conductivity of the **bis-NAD-10** samples is determined to be equal to 0.031 W m^{-1} K^{-1}, which compares favorably with that of polyurea cross-linked silica aerogels (0.041 W m^{-1} K^{-1} at 0.451 g cm^{-3}),[42] glass wool (0.040 W m^{-1} K^{-1}), styrofoam (0.030 W m^{-1} K^{-1}), and polyurethane foam (0.026 W m^{-1} K^{-1}).[53]

4. CONCLUSIONS

Bis-NAD-xx aerogels, considered together with other organic aerogels from the recent literature,[8−17] exemplify the design parameters for the bottom-up synthesis of polymeric gels that can be dried to aerogels. The key requirement seems to be phase separation of surface-reactive nanoparticles that can cross-link with each other into a three-dimensional network. Phase separation is induced by reduced solubility of the growing polymer, which, in turn, is introduced by cross-linking at the molecular level.

Significant shrinking (in the present case, up to 40%) seems to be encountered more frequently with organic aerogels rather than their inorganic counterparts. Although that is typically a problem with the latter, leading to cracking, the more-flexible organic framework seems to accommodate stresses better, and the materials come out as perfect monoliths. More importantly though, desirable properties such as high surface area, porosity, and pore structure do not seem to be affected detrimentally; in that regard, shrinkage may be difficult to predict, but most certainly is reproducible and therefore can be engineered into the final object. As demonstrated herewith, ROMP-derived

dx.doi.org/10.1021/cm200323e |Chem. Mater. 2011, 23, 2250–2261

polyimide aerogels can be prepared in one step as mesoporous materials over a wide density range with high porosities, high surface areas, high modulus, high strength, and high toughness. Combining the one-step synthesis with mechanical strength, manageable thermal stability, relatively low thermal conductivity, and low speed of sound wave propagation render **bis-NAD-xx** to be reasonable multifunctional candidates for further investigation into thermal and acoustic insulation at elevated temperatures. From a theoretical perspective, **bis-NAD-xx** emphasize the fact that nucleation and network growth in organic aerogels is a complicated process that may not be known *a priori*, but it has definite effects on the performance of the materials. It can be influenced by typical reaction conditions, such as solvent, temperature, monomer, and catalyst concentration; moreover, predictability most certainly can be gained through multivariable optimization studies.

AUTHOR INFORMATION

Corresponding Authors:
*E-mail address: (N.L.) leventis@mst.edu; (C.S.-L.) cslevent@mst.edu; (J.T.M.) jtmang@lanl.gov; (H.L.) hongbing.lu@utdallas.edu.

ACKNOWLEDGMENT

We thank the following for their financial support: the Army Research Office, under Award No. W911NF-10-1-0476 (N.L., C. S.-L.); and the National Science Foundation, under Agreement Nos. CHE-0809562 (N.L., C.S.-L.), DMR-0907291 (N.L., H.L.), CMMI-0653970 (N.L., C.S.-L.), and CMMI-0653919 (H.L.). We also acknowledge the Materials Research Center of Missouri S&T for its support in sample characterization (SEM, XRD). Solids NMR work was conducted at the University of Missouri Columbia by Dr. Wei Wycoff. This work also benefited from the use of the SANS instrument, LQD at the Manuel Lujan, Jr. Neutron Scattering Center of the Los Alamos National Laboratory, supported by the DOE Office of Basic Energy Sciences; this work also utilized facilities supported in part by the National Science Foundation, under Agreement No. DMR-0454672.

REFERENCES

(1) Pierre, A. C.; Pajonk, G. M. *Chem. Rev.* **2002**, *102*, 4243–4265.
(2) Morris, C. A.; Anderson, M. L.; Stroud, R. M.; Merzbacher, C. I.; Rolison, D. R. *Science* **1999**, *284*, 622–624.
(3) Kistler, S. S. *Nature* **1931**, *127*, 741.
(4) Kistler, S. S. *J. Phys. Chem.* **1932**, *36*, 52–63.
(5) Gash, A. E.; Pantoya, M.; Satcher, J. H.; Simpson, R. L. *Polym. Prepr. (Am. Chem. Soc., Div. Polym. Chem.)* **2008**, *49*, 558–559.
(6) Leventis, N.; Chandrasekaran, N.; Sadekar, A. G.; Mulik, S.; Sotiriou-Leventis, C. *J. Mater. Chem.* **2010**, *20*, 7456–7471.
(7) Baumann, T. F.; Gash, A. E.; Chinn, S. C.; Sawvel, A. M.; Maxwell, R. S.; Satcher, J. H., Jr. *Chem. Mater.* **2005**, *17*, 395–401.
(8) Pekala, R. W. *Low Density Resorsinol–Formaldehyde Aerogels*, U.S. Patent No. 4,873,218, 1989.
(9) Pekala, R. W.; Alviso, C. T.; Lu, X.; Gross, J.; Frickle, J. *J. Non-Cryst. Solids* **1995**, *188*, 34–40.
(10) Li, W.-C.; Lu, A.-H.; Guo, S.-C. *J. Colloidal Interface Sci.* **2002**, *254*, 153–157.
(11) Pekala, R. W. *Melamine–Formaldehyde Aerogels*, U.S. Patent No. 5,086,085, 1992.
(12) Biesmans, G.; Martens, A.; Duffours, L.; Woignier, T.; Phalippou, J. *J. Non-Cryst. Solids* **1998**, *225*, 64–68.
(13) Lee, J. K.; Gould, G. L.; Rhine, W. L. *J. Sol–Gel Sci. Technol.* **2009**, *49*, 209–220.
(14) Lorjai, P.; Chaisuwan, T.; Wongkasemjit, S. *J. Sol–Gel Sci. Technol.* **2009**, *52*, 56–64.
(15) Lee, J. K.; Gould, G. L. *J. Sol–Gel Sci. Technol.* **2007**, *44*, 29–40.
(16) Rhine, W.; Wang, J.; Begag, R. *Polyimide Aerogels, Carbon Aerogels, and Metal Carbide Aerogels and Methods of Making Same*, U.S. Patent No. 7,074,880, 2006.
(17) (a) Kawagishi, K.; Saito, H.; Furukawa, H.; Horie, K. *Macromol. Rapid Commun.* **2007**, *28*, 96–100. (b) Meador, M. A. B.; Malow, E. J.; He, Z. J.; McCorkle, L.; Guo, H.; Nauyen, B. N. *Polym. Prepr. (Am. Chem. Soc., Div. Polym. Chem.)* **2010**, *51*, 265–266.
(18) Daniel, C.; Giudiee, S.; Guerra, G. *Chem. Mater.* **2009**, *21*, 1028–1034.
(19) Goueree, P.; Talbi, H.; Miousse, D.; Tran-van, F.; Dao, L. H.; Lee, K. H. *J. Electrochem. Soc.* **2001**, *148*, A94–A101.
(20) (a) Fischer, F.; Rigacci, A.; Pirard, R.; Berthon-Fabry, S.; Achard, P. *Polymer* **2006**, *47*, 7636–7645. (b) Gavillon, R.; Budtova, T. *Biomacromolecules* **2008**, *9*, 269–277. (c) Surapolchai, W.; Schiraldi, D. A. *Polym. Bull.* **2010**, *65*, 951–960.
(21) (a) Leventis, N.; Sotiriou-Leventis, C.; Zhang, G.; Rawashdeh, A.-M. M. *Nano Lett.* **2002**, *2*, 957–960. (b) Zhang, G.; Dass, A.; Rawashdeh, A.-M. M.; Thomas, J.; Counsil, J. A.; Sotiriou-Leventis, C.; Fabrizio, E. F.; Ilhan, F.; Vassilaras, P.; Scheiman, D. A.; McCorkle, L.; Palczer, A.; Johnston, J. C.; Meador, M. A. B.; Leventis, N. *J. Non-Cryst. Solids* **2004**, *350*, 152–164. (c) Leventis, N.; Palczer, A.; McCorkle, L.; Zhang, G.; Sotiriou-Leventis, C. *J. Sol–Gel Sci. Technol.* **2005**, *35*, 99–105. (d) Leventis, N. *Acc. Chem. Res.* **2007**, *40*, 874–884. (e) Leventis, N.; Vassilaras, P.; Fabrizio, E. F.; Dass, A. *J. Mater. Chem.* **2007**, *17*, 1502–1508. (f) Leventis, N.; Mulik, S.; Sotiriou-Leventis *Chem. Mater.* **2008**, *20*, 6985–6997.
(22) Sroog, C. E.; Endrey, A. L.; Abrmo, S. V.; Berr, C. E.; Edward, W. M.; Oliver, K. L. *J. Polym. Sci., Part A* **1965**, *3*, 1373–1390.
(23) (a) Edward, W. M.; Robinson, I. M. *Polyimides of Pyromellitic Acid*, U.S. Patent No. 2,710,853, 1955. (b) Edwards, W. M.; Robinson, I. M. *Preparation of Pyromellitimides*, U.S. Patent No. 2,867,609, 1959.
(24) (a) Woodfine, B.; Soutar, I.; Preston, P. N.; Jigajinni, V. B.; Stewart, N. J.; Hay, J. N. *Macromolecules* **1993**, *26*, 6330–6334. (b) Baugher, A. H.; Espe, M. P.; Goetz, J. M.; Schaefer, J.; Pater, R. H. *Macromolecules* **1997**, *30*, 6295–6301. (c) Hu, A. J.; Hao, J. Y.; He, T.; Yang, S. Y. *Macromolecules* **1999**, *32*, 8046–8051. (d) Xie, W.; Pan, W.-P.; Chuang, K. C. *Thermochim. Acta* **2001**, *367–368*, 143–153.
(25) Sroog, C. E. *Prog. Polym. Sci.* **1991**, *16*, 561–694.
(26) Chidambareswarapattar, C.; Larimore, Z.; Sotiriou-Leventis, C.; Mang, J. T.; Leventis, N. *J. Mater. Chem.* **2010**, *20*, 9666–9678.
(27) Grubbs, R. H. *Angew. Chem., Int. Ed.* **2006**, *45*, 3760–3765.
(28) (a) Laguitton, B.; Mison, P.; Sillion, B.; Brisson, J. *Macromolecules* **1998**, *31*, 7203–7207. (b) Chen, C.-F.; Qin, W.-M.; Huang, X.-A. *Polym. Eng. Sci.* **2008**, *48*, 1151–1156.
(29) Seeger, P. A.; Hjelm, R. P., Jr. *J. Appl. Crystallogr.* **1991**, *24*, 467–478.
(30) Liu, Y.; Sun, X. D.; Xie, X.-Q.; Scola, D. A. *J. Polym. Sci., Part A: Polym. Chem.* **1998**, *36*, 2653–2665.
(31) The polymerization of **bis-NAD** via ROMP is expected to be a living process that proceeds until all of the monomer is consumed. For example, see: Bielawski, C. W.; Grubbs, R. H. *Prog. Polym. Sci.* **2007**, *32*, 1–29.
(32) (a) Everett, D. H. *Basic Principles of Colloid Science*; The Royal Society of Chemistry: London, U.K., 1988; p 189. (b) Ilmain, F.; Tanaka, T.; Kokufuta, E. *Nature* **1991**, *349*, 400–401.
(33) Sing, K. S. W.; Everett, D. H.; Haul, R. A. W.; Moscou, L.; Pierotti, R. A.; Rouquerol, J.; Siemieniewska, T. *Pure Appl. Chem.* **1985**, *57*, 603–619.
(34) Lowell, S.; Shields, J. E.; Thomas, M. A.; Thommes, M. *Characterization of Porous Solids and Powders: Surface Area, Pore Size and Density*; Kluwer Academic Publishers: Norwell, MA, 2004; pp 44–45.
(35) Webb, P. A.; Orr, C. *Analytical Methods in Fine Particle Technology*; Micromeritics Instrument Corporation: Norcross, GA, 1997; pp 67–68.
(36) (a) Beaucage, G. *J. Appl. Crystallogr.* **1995**, *28*, 717–728. (b) Beaucage, G. *J. Appl. Crystallogr.* **1996**, *29*, 134–146. (c) Mang,

J. T.; Son, S. F.; Hjelm, R. P.; Peterson, P. D.; Jorgensen, B. S. *J. Mater. Res.* **2007**, *22*, 1907–1920. (d) Tappan, B. C.; Huynh, M. H.; Hiskey, M. A.; Chavez, D. E.; Luther, E. P.; Mang, J. T.; Son, S. F. *J. Am. Chem. Soc.* **2006**, *128*, 6589–6594.

(37) Orcel, G.; Gould, R. W.; Hench, L. L. In *Better Ceramics Through Chemistry II*; Brinker, C. J., Clark, D. E., Ulrich, D. R., Eds.; Materials Research Society: Pittsburgh, PA, 1986; Vol. 73, p 289.

(38) Hench, L. L.; West, J. K. *Chem. Rev.* **1990**, *90*, 33–72.

(39) (a) Zallen, R. *The Physics of Amorphous Solids*; Wiley: New York, 1983; Chapter 4. (b) Stauffer, D.; Conialio, A.; Adam, M. *Adu. Polym. Sci.* **1982**, *44*, 103.

(40) Daphalapurkar, N. P.; Hanan, J. C.; Phelps, N. B.; Bale, H.; Lu, H. *Mech. Adv. Mater. Struct.* **2008**, *15*, 594–611.

(41) (a) Fricke, J. *J. Non-Cryst. Solids* **1988**, *100*, 169–173. (b) Gross, J.; Fricke, J. *Nanostructured Mater.* **1995**, *6*, 905–908. (c) Luo, H.; Churu, G.; Schnobrich, J.; Hobbs, A.; Fabrizio, E. F.; Dass, A.; Mulik, S.; Sotiriou-Leventis, C.; Lu, H.; Leventis, N. *J. Sol−Gel Sci. Technol.* **2008**, *48*, 113–134.

(42) Katti, A.; Shimpi, N.; Roy, S.; Lu, H.; Fabrizio, E. F.; Dass, A.; Capadona, L. A.; Leventis, N. *Chem. Mater.* **2006**, *18*, 285–296.

(43) Leventis, N.; Sotiriou-Leventis, C.; Chandrasekaran, N.; Mulik, S.; Larimore, Z. J.; Lu, H.; Churu, G.; Mang, J. T. *Chem. Mater.* **2010**, *22*, 6692–6710.

(44) Meador, M. A. B.; Fabrizio, E. F.; Ilhan, F.; Dass, A.; Zhang, G.; Vassilaras, P.; Johnston, J. C.; Leventis, N. *Chem. Mater.* **2005**, *17*, 1085–1098.

(45) Meador, M. A. B.; Capadona, L. A.; MacCorkle, L.; Papadopoulos, D. S.; Leventis, N. *Chem. Mater.* **2007**, *19*, 2247–2260.

(46) Mulik, S.; Sotiriou-Leventis, C.; Churu, G.; Lu, H.; Leventis, N. *Chem. Mater.* **2008**, *20*, 5035–5046.

(47) Woignier, T.; Reynes, J.; Hafili-Alaoui, A.; Beurroies, I.; Phalippou, J. *J. Non-Cryst. Solids* **1998**, *241*, 45–52.

(48) (a) American Society for Metals. *ASM Engineering Materials Handbook, Composites*, Vol. 1; ASM International: Materials Park, OH, 1998; p 178, Table 2. (b) Luo, H.; Chen, W. *Intern. J. Appl. Ceram. Technol.* **2004**, *1*, 254–260. (c) Luo, H.; Chen, W.; Rajendran, A. M. *J. Am. Ceram. Soc.* **2006**, *89*, 266–273.

(49) Hogg, P. J. *Science* **2006**, *314*, 1100–1101.

(50) Parker, W. J.; Jenkins, J. J.; Abbott, G. L.; Butler, C. P. *J. Appl. Phys.* **1961**, *32*, 1679–1684.

(51) Lee, D.; Stevens, P. C.; Zeng, S. Q.; Hunt, A. J. *J. Non-Cryst. Solids* **1995**, *186*, 285–290.

(52) (a) Cowan, R. *J. Appl. Phys.* **1961**, *32*, 1363–1369. (b) Cowan, R. *J. Appl. Phys.* **1963**, *34*, 926–927.

(53) Lide, D. R. *CRC Handbook of Chemistry and Physics*, 84th ed.; CRC Press: Boca Raton, FL, 2003; pp 12/22612/227.